Faraday Discussions

ROYAL SOCIETY
OF CHEMISTRY

PAPER

View Article Online
View Journal | View Issue

A facile two-step method for fabrication of plate-like WO₃ photoanode under mild conditions†

Nan Wang,[ab] Jian Zhu,[ab] Xiaojia Zheng,[ab] Fengqiang Xiong,[ab] Baokun Huang,[a] Jingying Shi*[a] and Can Li*[a]

Fabrication of photoelectrodes on a large-scale, with low-cost and high efficiency is a challenge for their practical application in photoelectrochemical (PEC) water splitting. In this work, a typical plate-like WO₃ photoanode was fabricated with chemical etching of the as-prepared mixed tungsten−metal oxides (W−M−O, M = Cu, Zn or Al) by a reactive magnetron co-sputtering technique, which results in a greatly enhanced PEC performance for water oxidation in comparison with that obtained from a conventional magnetron sputtering method. The current approach is applicable for the fabrication of some other semiconductor photoelectrodes and is promising for the scaling up of applications for highly efficient solar energy conversion systems.

1 Introduction

Photoelectrochemical (PEC) water splitting has been regarded as a promising way to produce hydrogen from water and solar energy.[1–3] The photoelectrode, a conductive, substrate-supported semiconductor thin-film material, in general, is the crucial part of a photoelectrolysis cell. Depending on the techniques and preparation conditions, photoelectrodes may present different structural, optical and electrical behaviors, and consequently different PEC performances.

The reactive magnetron sputtering technique has been used widely in industry for preparing large-area and uniform films well connected to the substrates. The structure of the deposited film can be easily controlled by adjusting the process parameters, and it is also quite easy to repeat the production process. Hence, this technique shows huge potential for practical, large-scale manufacturing of thin-film materials. Some metal oxide or oxynitride photoelectrodes such as TiO₂,[4]

aState Key Laboratory of Catalysis, Dalian Institute of Chemical Physics, Dalian National Laboratory for Clean Energy, Chinese Academy of Sciences, 457 Zhongshan Road, Dalian 116023, China. E-mail: canli@dicp.ac.cn; jingyingshi@dicp.ac.cn; Fax: +86 411 84694447; Tel: +86 411 84379070

bUniversity of Chinese Academy of Sciences, Beijing, 100049, China

WO_3,[5] $BiVO_4$,[6] and TaON[7] have been prepared by this method for PEC water splitting, and showed good stability and anti-corrosion properties in electrolyte. However, these films generally present a mirror-like surface as well as a compact structure that result in high reflectivity and a small contact surface area with the electrolyte, which make their PEC water-splitting performances greatly limited. To overcome this shortcoming, we intentionally introduce other metal oxides through magnetron co-sputtering and subsequently remove the impurity phase by chemical etching to fabricate porous photoelectrodes with higher PEC activity.

WO_3 is a well-known semiconductor material for photoanodes as it can absorb within the visible light region and shows a remarkable stability in acidic solutions.[8,9] Porous WO_3 photoanodes can be fabricated generally through liquid-phase routes. For example, Amal *et al.*[10] prepared flower-like nanostructured tungsten oxide hydrate thin films by electrochemical anodization of tungsten foil at high potentials. Widenkvist *et al.*[11] obtained plate-like $WO_3 \cdot H_2O$ films on a tungsten substrate in acid medium at temperatures higher than 50 °C. The groups of Yang[12] and Demir[13] synthesized tungsten trioxide hydrate ($WO_3 \cdot 1/3H_2O$) films *via* conventional hydrothermal technology at higher than 120 °C. Recently our group successfully fabricated the hexagonal nanoflower $WO_3 \cdot 1/3H_2O$ array on fluorine-doped tin oxide (FTO) substrates by a microwave-assisted hydrothermal method.[14] All of the above as-prepared WO_3 hydrate ($WO_3 \cdot nH_2O$) thin films can be converted into the WO_3 phase *via* calcination at about 450 °C without changing the morphology. In other words, nanocrystalline WO_3 films prepared by these liquid-phase synthesis methods possess porous network structures, and often exhibit a large surface area as well as enhanced light absorbance. However, these wet chemical synthesis routes usually need high reaction temperatures or high anodization voltages which are difficult to operate in a large scale.

In this work, some impurity metals (M = Cu, Zn or Al) were sputtered together with tungsten to produce mixed tungsten–metal oxides (W–M–O) thin films on FTO glass substrates. After soaking in an acidic solution of HCl, H_2SO_4 or HNO_3 for etching at room temperature, these extra metal oxides disappeared due to dissolution in the acidic media while a porous plate-like WO_3 phase, distinct from conventional compact WO_3 thin films prepared by a magnetron sputtering, was left behind with twice photocurrent enhancement for PEC water oxidation. This approach can be applied generally and useful for the fabrication of some other semiconductor photoelectrodes.

2 Experimental

Sample preparation

Samples of W–M–O films (M = Cu, Al or Zn) were deposited on commercial FTO (NSG, sheet resistance of 20 Ω $\square^{-1}$) glass substrates by reactive magnetron co-sputtering system (PVD75, Kurt J. Lesker Company). The FTO glass substrates were cleaned in acetone–isopropanol–ethanol–DI water in sequence. The co-sputtering system consists of two DC guns, loaded with a 99.95% pure W target and 99.99% pure Cu (or 99.99% pure Zn, 99.99% pure Al) target, respectively. The target–substrate distance was fixed at 170 mm. Both targets have a diameter of 3 inches and a thickness of 3 mm. After pressure had been pumped down to 7×10^{-7} torr, the O_2 and Ar gases (99.99% purities) were introduced into the chamber through mass flow controllers and the gas flow was set for an $[O_2]/([Ar] + [O_2])$ ratio

of 38%. The oxygen partial pressure and the total sputtering pressure were 2 and 10 mtorr, respectively. The sputtering power of the tungsten target was fixed at about 150 W while the M content in the films was controlled by varying the sputtering power applied to the M target. The sputtering power was 60, 60 and 70 W for Zn, Al and Cu targets, respectively. The as-sputtered samples were immersed in an aqueous solution of H_2SO_4, HNO_3 or HCl for various periods of time. Subsequently, the as-etched photoelectrodes were washed with deionized (DI) water and then calcined in air at 500 °C for 2 h.

Characterization

The crystal structure was measured by X-ray powder diffraction (XRD, Rigaku D/Max-2500/PC powder diffractometer) using Cu Kα radiation ($\lambda = 0.15406$ nm) with an operating voltage of 40 kV and an operating current of 200 mA. The scan rate is 5° min^{-1} in the range of 10–60°. The surface morphology and dopant concentration were measured by scanning electron microscopy (SEM, Quanta 200 FEG). The surface profile was used to characterize the film thickness and the roughness (Dektak 150 Surface Profiler, Veeco). Optical properties were measured using an Agilent Cary 5000 UV-Vis spectrophotometer. Raman spectra were collected using a Renishaw inVia Raman spectrometer excited by a solid laser (532 nm), and the spectral resolution was 1.5–2 cm^{-1}. In order to investigate the chemical bonding and dopant concentration, X-ray photoelectron spectroscopy (XPS) were made using a KROTOS AMICAS spectrometer (Shimadzu, Japan) with a magnesium Kα X-ray source. The carbon C 1s line position at 284.8 eV was used as a reference to correct the charging effect. The as-sputtered W–Zn–O and W–Cu–O films and the samples after etching in 1 M H_2SO_4 for 12 h were washed in 1 M KOH solution (10 mL). The size of each electrode was fixed at 15 mm × 20 mm and the thickness was about 1 μm. W, Cu and Zn concentrations of leached solutions were analyzed by inductively coupled plasma atomic emission spectrometry (ICP-AES) on a Shimadzu ICPS-8100 spectrometer.

Photoelectrochemical measurement

The photoelectrochemical properties were measured using a CHI electrochemical analyser (CHI 440B, CH Instruments, Inc.). Chopped I–V curves of the as-prepared thin films were obtained under simulated AM 1.5 solar illumination (100 mW cm^{-2}) using a three-electrode setup which had the as-prepared samples as the working electrode, platinum foil as the counter electrode, and a saturated calomel electrode (SCE) as the reference electrode in 0.5 M Na_2SO_4 (pH 3.0) with scan rate of 20 mV s^{-1}. Electrochemical impedance spectra (EIS) were measured in the frequency range of 100 kHz to 100 mHz and with an AC amplitude of 10 mV using an electrochemical workstation (IM6 Zahner, Germany). The relative electrochemical surface area (ECSA) was determined from capacitance measurements carried out in the dark by cyclic voltammetry in the region between 0.15 and 0.35 V $vs.$ SCE in 0.5 M Na_2SO_4 (pH 3.0), and the scan rates were varied between 25 and 300 mV s^{-1}.

3   Results and discussion

Fig. 1a exhibits the XRD patterns for the as-sputtered samples etched in 1 M H_2SO_4 aqueous solution for different time intervals. Besides the characteristic diffraction peaks represent for the FTO substrate, a broad peak in the range of 15–35° clearly indicates an amorphous phase for the as-sputtered film. Hardly any new phase can be detected when the sample was etched for only 1 h, whereas a new diffraction peak located at about 12.7° appeared after soaking for 2 h. Extending the etching time to 3–12 h, the diffraction peaks corresponding to $WO_3 \cdot 2H_2O$ (JCPDS card no. 18-1420, monoclinic, $P2/m(10)$) can be clearly observed. The increased diffraction intensity and the narrowed full width at half-maximum (FWHM) of the characteristic peaks with etching time suggest an improved crystallinity and a larger grain size. After being calcined at 500 °C for 2 h, the XRD patterns for the corresponding samples are shown in Fig. 1b. Clearly, the mixed crystallized phases of WO_3 and $CuWO_4$ (JCPDS card no. 43-1035 and no. 72-0616) are present when the etching time is shorter than 5 h, whereas a pure monoclinic WO_3 phase is be achieved after the as-sputtered sample was further corroded for a period of 6 h or more. These results may suggest that the residual copper can react with tungsten oxide to produce $CuWO_4$ in the calcination process and that the impurity copper can be completely removed by etching.

The phase transformation of the surface region was further investigated by Raman spectroscopy (in Fig. 2). Compared with the Raman spectrum of the blank FTO substrate (Fig. S1†), the bands at 552 and 1097 cm^{-1} originate from the FTO substrate so those at 798 and 956 cm^{-1} should be assigned to W–Cu–O compound for the as-sputtered sample, which is also different from the Raman bands for the as-sputtered tungsten oxide (Fig. S1†). This result obviously indicates the successful introduction of the copper impurity by co-sputtering. The signals from
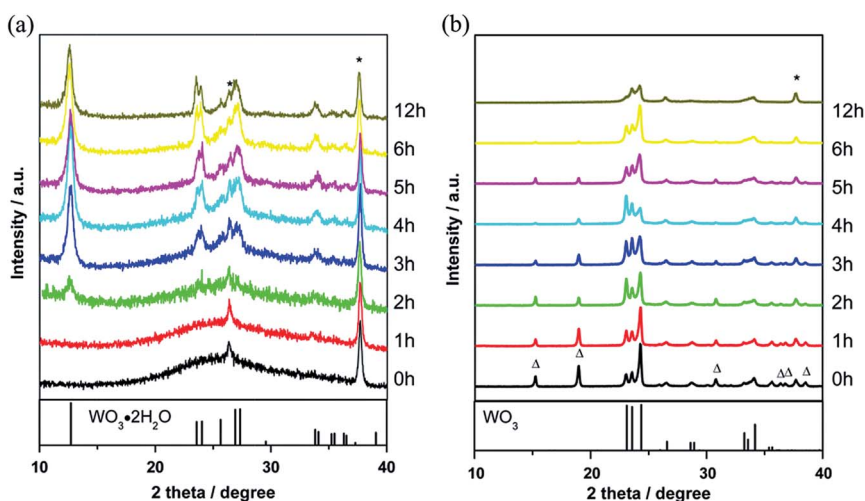

Fig. 1   (a) XRD patterns for the as-sputtered samples etched in 1 M H_2SO_4 aqueous solution for various periods. (b) XRD patterns of etched W−Cu−O samples after calcination in air at 500 °C for 2 h. The peaks marked with △ are assigned to $CuWO_4$ and the peaks marked with * to the FTO substrate.
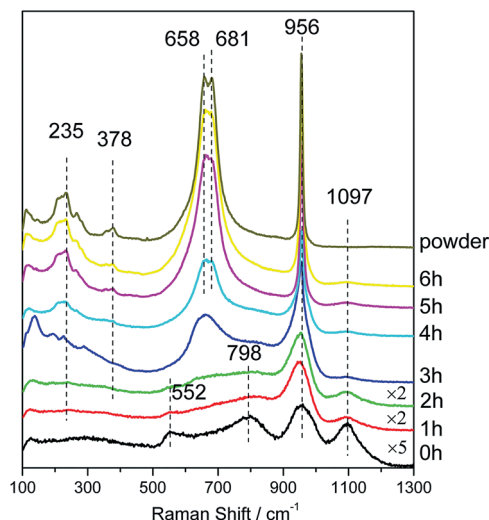
Fig. 2 Raman spectra of samples prepared at different etching times and the precipitation in the solutions.

the substrate as well as the intensity of the band at 798 cm^{-1} become weak when the etching time is within 2 h. However, the Raman scattering at 956 cm^{-1}, which originates from the symmetric stretching mode of the terminal W=O bond, stays at the same intensity. Extending the etching time to 3 h, the band at about 645 cm^{-1} appears, indicating that the oxide is gradually converted into $WO_3 \cdot H_2O$.[15] This broad band is blue-shifted to 670 cm^{-1} which is assignable to the stretching mode of the W–O–W bonds, gaining higher intensity with increasing etching time to 4 h. As the time is prolonged to 5 h, this band splits into two bands at 658 and 681 cm^{-1}, respectively, which may indicate the $WO_3 \cdot H_2O$ phase had evolved into $WO_3 \cdot 2H_2O$. Moreover, the signal from the W=O bond at 956 cm^{-1} is greatly enhanced. On the other hand, the lower frequency bands at 378 cm^{-1} (W–OH$_2$ vibration) and 235 cm^{-1} (W–O–W bending vibration) appear. These bands are significantly influenced by the degree of hydration and can be used as a spectral marker to determine the hydration level of WO_3.[15,16] The yellowish precipitate present in the etching solution was also collected for Raman measurement and it shows a doublet of narrow bands at 658 and 681 cm^{-1} corresponding to $WO_3 \cdot 2H_2O$.

The surface morphologies observed by SEM at different chemical etching time intervals are illustrated in Fig. 3. The as-sputtered sample shows a compact morphology (Fig. 3a) which is similar to film materials deposited using a single magnetron sputtering technique.[5,17] After one hour's etching, small pinholes and cracks appear at random, together with some platelets present on the surface as shown in Fig. 3b. When the etching time was increased to 2 h, the number of cracks and the width of gaps developed. The platelets aggregated to form spheroidal structures (Fig. 3c). Upon further extension of the etching time, these spheroidal structures became larger until they covered the whole surface with a diameter of about 1 μm and the thickness of each platelet is about 80 nm, while pores and cracks vanish gradually when the etching time is extended to 5 h

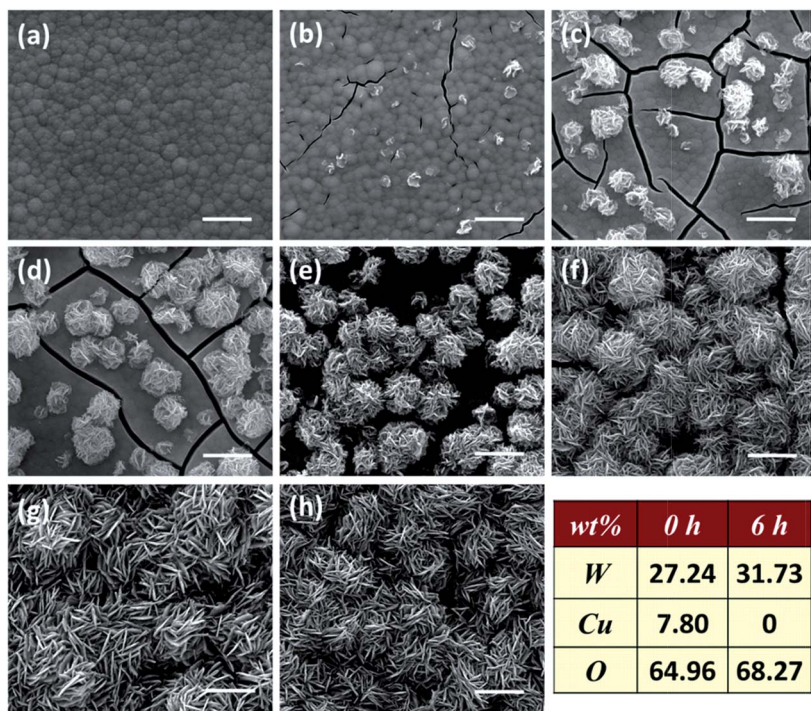| wt%	0 h	6 h
W	27.24	31.73
Cu	7.80	0
O	64.96	68.27

Fig. 3 SEM images of amorphous W–Cu–O films with different chemical etching durations to investigate the growth of plate-like structures: (a) 0 h, (b) 1 h, (c) 2 h, (d) 3 h, (e) 4 h, (f) 5 h, (g) 6 h, (h) 48 h and EDX elemental analysis. Scale bar: 1 μm.

(Fig. 3d–f). The plate-like morphology and particle size remain almost unchanged even after a longer etching time of up to 48 h (Fig. 3g and 3h). The element atom ratios detected by EDX analysis are listed in the inserted table, and it can be seen that the W element remains present while the content of Cu decreases to the detection limit after etching for 6 h. The cross-sectional SEM images for samples in Fig. 3 were also detected and the are results shown in Fig. 4. It is observed that the platelets appear on the surface and then permeate to the bulk of film gradually without significant change of the film thickness, which implies that the dissolution and crystallization proceed simultaneously.

For comparison, the as-sputtered tungsten oxide film was also immersed into acid solution for several hours. The compact film seems to be marginally dissolved after treatment for 6 h, as seen *via* SEM observation in Fig. S2,† showing a much slower reaction rate than the amorphous W–M–O films etched in acid solution presented in Fig. 3, Fig. S3 and S4,† which means the presence of the impurity metal can accelerate the corrosion process.

The chemical surface states of the as-sputtered W–Cu–O films before and after etching were characterized by X-ray photoelectron spectroscopy (XPS) as shown in Fig. 5. Before etching, the two main peaks of Cu 2p located at 932.0 and 951.9 eV correspond to Cu $2p_{3/2}$ and Cu $2p_{1/2}$, and the satellite peaks on the high-energy side are clearly observed. After etching, there are no Cu signals detected (in Fig. 5a). Spectra of the W 4f peaks presented in Fig. 5b are dominated by a
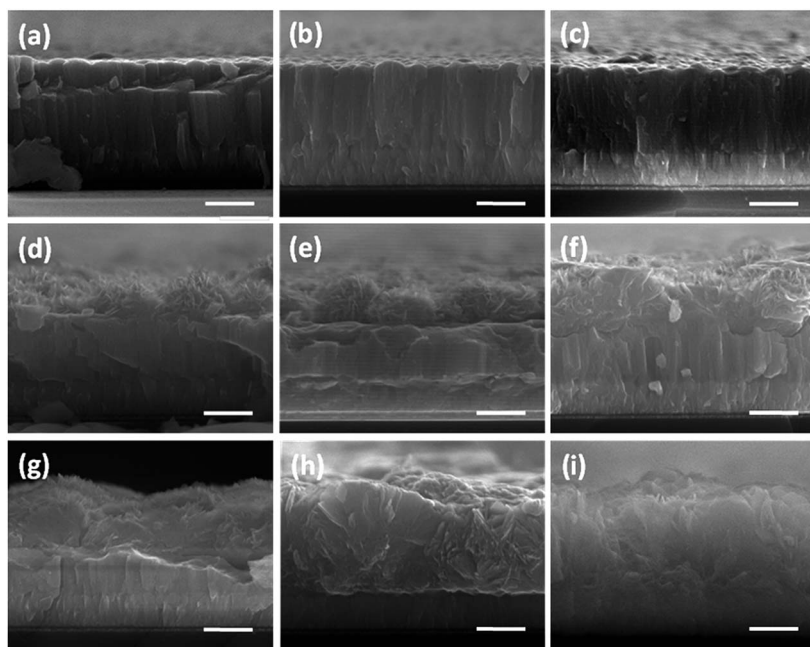
Fig. 4 Cross-section SEM images of amorphous W–Cu–O films after different chemical etching durations: (a) 0 h, (b) 1 h, (c) 2 h, (d) 3 h, (e) 4 h, (f) 5 h, (g) 6 h, (h) 12 h and (i) 48 h. Scale bar: 500 nm.

spin–orbit doublet at binding energies of 37.85 eV (W $4f_{5/2}$) and 35.70 eV (W $4f_{7/2}$), which are associated with the W^{6+} oxidation state. The O 1s spectrum of the as-prepared sample shows a peak located at 530.7 eV in Fig. 5c, which corresponds to W=O bonding modes. And a small peak appears in the region at 533.1 eV after etching, which is also the signal from H_2O molecules bound with WO_3.[15]
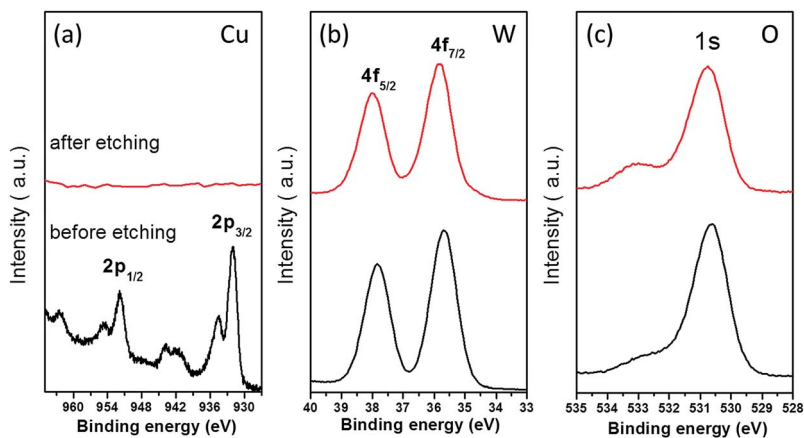

Fig. 5 XPS spectra of the as-sputtered film before and after etching: (a) Cu 2p, (b) W 4f and (c) O 1s.

Instead of copper, aluminum and zinc were also used as the impurity metal sources for reactive magnetron co-sputtering to deposit W–Al–O and W–Zn–O mixed oxide films onto FTO substrates. During the chemical etching process in acidic solution, similar morphology evolutions were observed, from the compact surface, to pinholes and cracks, to a final plate-like aggregated crystal structure (as shown in Fig. S2 and S3†). Further SEM studies investigated the influence of the acid concentration on the shape and size variation, as shown in Fig. 6. It reveals that the quantity of acid plays an important role in determining the final morphology of the electrode. In 0.5 M HCl aqueous solution, some large plate structures are obtained (Fig. 6a). Increasing the concentration of HCl to 1.0 M, there are middle-sized agglomerated plates on the surface (Fig. 6b). It is also observed that aggregation of plates with a smaller size are obtained when the concentration of HCl is further increased (Fig. 6c and d), which demonstrates that the number of nuclei formed increases as well as the size of particles decreases. The difference of shape can be explained in the form of the different growth rates of different crystal faces.[18] The SEM images of the obtained photoanodes prepared using different impurity metals under the same acid solution concentration in the etching process are compared in Fig. S5,† which reveals almost the same size and thickness with similar plate-like morphologies. These results indicate that this method is a general approach toward the fabrication of plate-like tungsten oxide hydrate. Compared with conventional hydrothermal synthesis or anodizing approaches, the etching method is effective and operative at ambient temperature and atmospheric pressure.
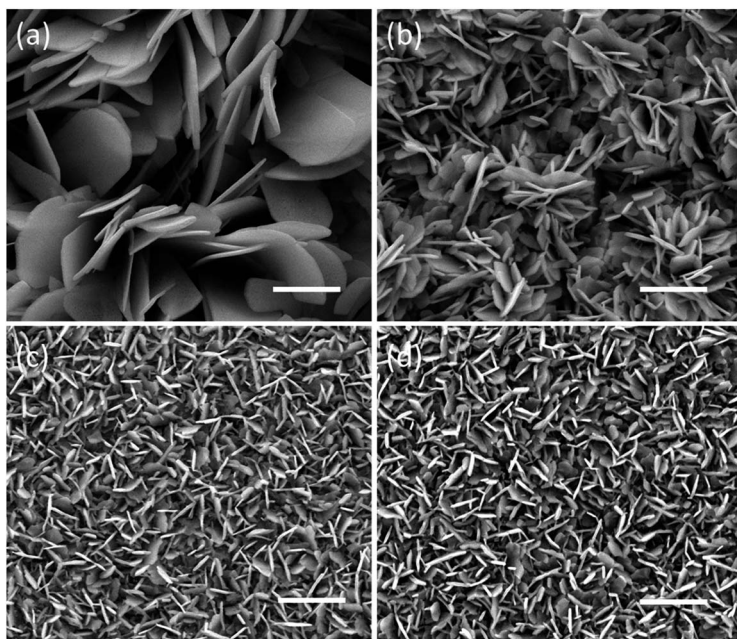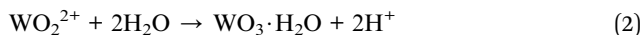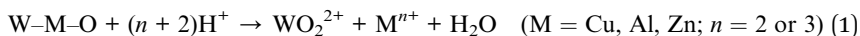

Fig. 6   SEM images of W−Cu−O film etched in (a) 0.5 M HCl, (b) 1 M HCl, (c) 2 M HCl and (d) 4 M HCl at room temperature; scale bars: 1 μm.

In order to verify the purity of product, the compositions of the as-sputtered sample and etched sample (12 h) were further detected *via* ICP-AES analysis. The Cu/W molar ratio of the W–Cu–O film decreased from 32.65 to 0.3%, and similarly the Zn/W molar ratio of the W–Zn–O film decreased from 17.72 to 0.03% (as listed in Table S1†), which confirms the removal of the impurity metal sources as indicated above.

Based on the above experimental results, we propose that the growth of $WO_3 \cdot 2H_2O$ crystal follows the dissolution–recrystallization mechanism during chemical etching at room temperature, which can be described by the following reactions:

$$W–M–O + (n + 2)H^+ \rightarrow WO_2^{2+} + M^{n+} + H_2O \quad (M = Cu, Al, Zn; n = 2 \text{ or } 3) \quad (1)$$

$$WO_2^{2+} + 2H_2O \rightarrow WO_3 \cdot H_2O + 2H^+ \quad (2)$$

$$WO_3 \cdot H_2O + H_2O \rightarrow WO_3 \cdot 2H_2O \quad (3)$$

When soaking in the strongly acidic aqueous solution, the as-the sputtered amorphous W–M–O film was gradually dissolved and tungsten element exists in the form of WO_2^{2+} (as has been reported in refs 19 and 20) and M^{n+} cations through corrosive pitting. The released WO_2^{2+} species quickly bond with the surrounding water molecules to form the insoluble $WO_3 \cdot H_2O$ nucleus while M^{n+} cations spread into the solution resulting in the leaching of impurity metal oxide. As the etching time goes on, WO_2^{2+} and M^{n+} cations are continuously produced so that the grain size of the $WO_3 \cdot H_2O$ crystals becomes increasingly larger and the M^{n+} cations simultaneously dissolve into the solution, leading to a final pure phase of tungsten oxide hydrate deposited on the surface. Certainly, it is reasonable for the $WO_3 \cdot H_2O$ to bond further with another H_2O molecule to convert into $WO_3 \cdot 2H_2O$ completely, as indicated by the above Raman analysis. A scheme for the formation mechanism of plate-like tungsten oxide hydrate ($WO_3 \cdot 2H_2O$) is shown in Fig. 7. In addition, it is noticed that the crystal size of the obtained $WO_3 \cdot 2H_2O$ increases with more dilute acidic solution as the etching medium, as observed above in Fig. 6. This is because the amount of WO_2^{2+} ions initially produced is smaller in a dilute acidic medium than that obtained in a more concentrated one, implying a smaller quantity of nucleation centers and a larger crystal size as a result. This phenomenon further confirms the above dissolution–recrystallization mechanism.
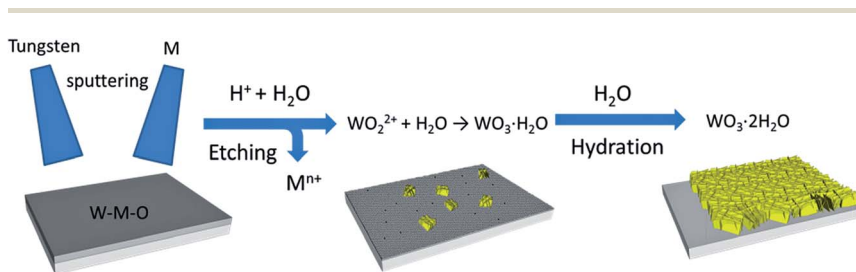

Fig. 7 Scheme for the formation mechanism of plate-like tungsten oxide hydrate ($WO_3 \cdot 2H_2O$).

Faraday Discussions

Fig. 8 compares the optical properties of the plate-like WO_3 film prepared by the current two-step method (Cu as the impurity source and etched in 1 M H_2SO_4 for 12 h) and the compact WO_3 deposited *via* the conventional magnetron sputtering technology, both thicknesses of which are controlled to be ~1 μm. It is seen from Fig. 8a that the optical transmittance for the plate-like films is under 20% in the visible-light range, which is much lower than that of the compact one (~60%). The surface roughness estimated from the reflectance property (Fig. 8b) by the profiler is 6.9 and 68.6 nm for compact and plate-like WO_3 films, respectively (shown in Fig. S6†), indicating an effective surface roughening by the etching treatment. Despite the higher light reflectance as shown in Fig. 8b, the porous WO_3 still has a much higher light absorption ability than the compact one (shown in Fig. 8c, evaluated according to the formula: $A = 100 - R - T$), which can be attributed to increased absorption paths among the plate-like structures.

The morphological change not only affects the roughness but also the surface area, which could play a major role in the reaction activity. The relative electrochemical surface area (ECSA) values of the electrodes are determined from the capacitive region of the cyclic voltammograms, as shown in Fig. 9. The measurements were carried out in the region between 0.15 and 0.35 V *vs.* SCE in 0.5 M Na_2SO_4 (pH 3.0) in the dark. Fig. 9a shows the capacitive current for the plate-like WO_3 film at six different scan rates from 25 to 300 mV s^{-1}, whereas the *C–V* curves of compact WO_3 and plate-like WO_3 photoanodes (scan rate = 50 mV s^{-1}) are compared in Fig. 9b. The linear relationships between the capacitive current and scan rate for the two electrodes are plotted in Fig. 9c. Assuming that the intrinsic specific surface capacitance of all the films is approximately the same, the relative surface area of the films can be determined.[21] The relative electrochemically active surface area of plate-like WO_3 is twice as large as the sputtered compact WO_3 film.

The photoelectrochemical behavior of the plate-like and compact WO_3 photoanodes was measured by obtaining the chopped light linear sweep voltammograms in 0.5 M Na_2SO_4 solution (pH 3.0), and these are compared in
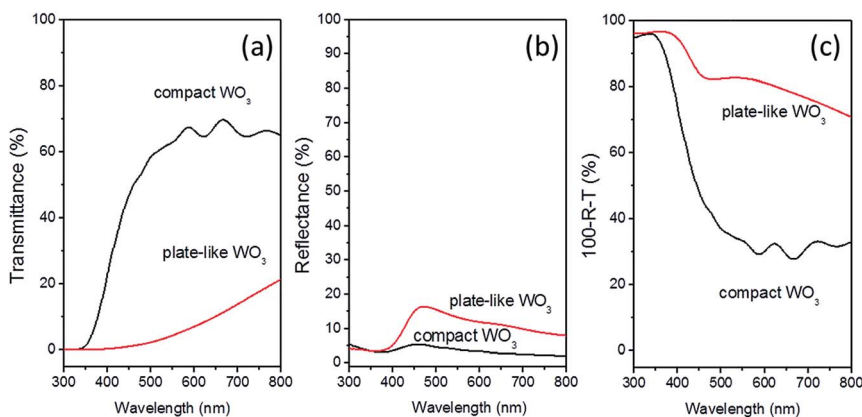

Fig. 8 UV-Vis spectra of compact WO_3 (black) and plate-like (red) WO_3 films grown on the FTO substrate. (a) Transmittance, (b) reflectance and (c) absorption ($100 - R - T$) spectra of the prepared photoelectrodes.
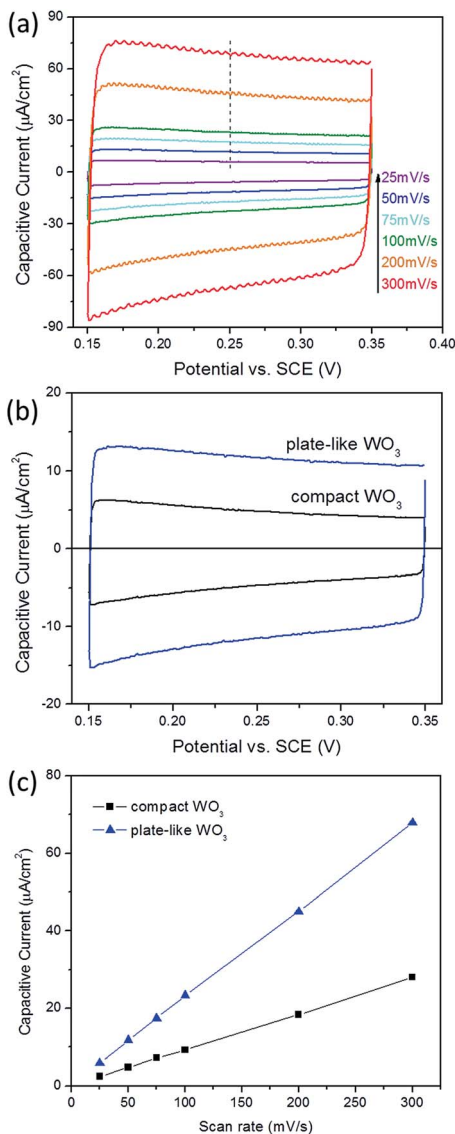
Fig. 9 (a) Cyclic voltammograms of plate-like WO_3 electrode tested at different scan rates. (b) $C-V$ curves of compact WO_3 and plate-like WO_3 electrodes (scan rate = 50 mV s^{-1}). (c) The linear relationship between the capacitive current and scan rate.

Fig. 10a. Clearly, the plate-like WO_3 electrode shows a higher saturation photocurrent density than the compact one although nearly the same onset potential of about 0.2 V *vs.* SCE is found for the two photoanodes. At the bias of 1.2 V *vs.* SCE, the photocurrent density generated over the porous sample is 0.95 mA cm^{-2}, which is almost twice of that generated over the compact one (0.58 mA cm^{-2}). In addition, the PEC performance of the samples prepared at different etching intervals following calcination in air at 500 °C was also measured, as shown in Fig. S7.† The photocurrent of the electrodes decreases with the shortening of the
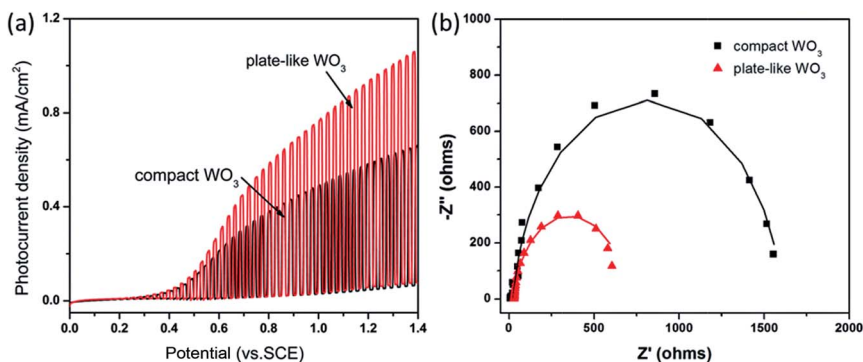
Fig. 10 (a) Linear sweep voltammetric scans of compact and plate-like WO$_3$ photoanodes in 0.5 M Na$_2$SO$_4$ (pH 3.0) under chopped AM 1.5G illumination; scanning rate: 20 mV s^{-1}. (b) Electrochemical impedance spectra and Nyquist plots of the compact and plate-like WO$_3$ photoanodes measured at 1.0 V vs. SCE in 0.5 M Na$_2$SO$_4$ solution (pH 3.0) under AM 1.5G illumination.

etching time and the as-sputtered W–Cu–O electrode without etching has the lowest photocurrent density, which reveals that the existence of Cu could be harmful to the PEC water oxidation reaction. After complete removal of the impurity metal, the saturation photocurrent density for the sample is 5-fold higher than that of un-etched one.

Electrochemical impedance spectroscopy was used to gain more insight into the reasons for the high photocurrent of the plate-like photoanode. The EIS spectra of compact WO$_3$ and plate-like WO$_3$ photoelectrodes measured under irradiation by AM 1.5G light (100 mW cm^{-2}), with a bias voltage of 1.0 V vs. SCE, are shown in Fig. 10b. The semicircle for compact WO$_3$ is larger than the plate-like WO$_3$ sample, indicating that the latter has a lower charge-transfer resistance. The fitted values of the solution resistance (R_s), charge-transfer resistance across the interface (R_p) and constant phase elements (CPE-T and CPE-P) were calculated and are listed in Table S2.† The fitted values of R_p are 1576 and 655.5 Ω for the compact WO$_3$ and plate-like WO$_3$ samples, respectively, implying that the plate-like structure is beneficial for this charge-transfer process.

Based on the above analysis, the improvement in the PEC water oxidation activity for the porous plate-like WO$_3$ photoanode can be mainly attributed to the increase of exposed surface area, light absorption and lower electrode/electrolyte interface charge-transfer resistance.

4 Conclusions

In this work, a porous plate-like tungsten oxide photoelectrode was successfully prepared on an FTO substrate by a facile two-step route including magnetron co-sputtering and chemical etching methods. The process of growth includes the dissolution of the as-sputtered amorphous W–M–O films in acidic medium, species precipitation and the recrystallization process. Compared to the compact WO$_3$ film counterparts, the photocurrent of PEC water oxidation with the plate-like WO$_3$ photoanode is improved significantly because the porous structure

provides more exposed surface area, increased light absorption and a lower electrode/electrolyte interface charge-transfer resistance.

Acknowledgements

References

1 M. G. Walter, E. L. Warren, J. R. McKone, S. W. Boettcher, Q. X. Mi, E. A. Santori and N. S. Lewis, *Chem. Rev.*, 2010, **110**, 6446–6473.

2 B. D. Alexander, P. J. Kulesza, I. Rutkowska, R. Solarska and J. Augustynski, *J. Mater. Chem.*, 2008, **18**, 2298.

3 H. M. Chen, C. K. Chen, R. S. Liu, L. Zhang, J. Zhang and D. P. Wilkinson, *Chem. Soc. Rev.*, 2012, **41**, 5654–5671.

4 H. Kikuchi, M. Kitano, M. Takeuchi, M. Matsuoka, M. Anpo and P. V. Kamat, *J. Phys. Chem. B*, 2006, **110**, 5537–5541.

5 B. Marsen, E. L. Miller, D. Paluselli and R. E. Rocheleau, *Int. J. Hydrogen Energy*, 2007, **32**, 3110–3115.

6 L. Chen, E. Alarcón-Lladó, M. Hettick, I. D. Sharp, Y. Lin, A. Javey and J. W. Ager, *J. Phys. Chem. C*, 2013, **117**, 21635–21642.

7 D. Yokoyama, H. Hashiguchi, K. Maeda, T. Minegishi, T. Takata, R. Abe, J. Kubota and K. Domen, *Thin Solid Films*, 2011, **519**, 2087–2092.

8 X. Liu, F. Wang and Q. Wang, *Phys. Chem. Chem. Phys.*, 2012, **14**, 7894–7911.

9 C. Santato, M. Odziemkowski, M. Ulmann and J. Augustynski, *J. Am. Chem. Soc.*, 2001, **123**, 10639–10649.

10 C. Ng, C. Ye, Y. H. Ng and R. Amal, *Cryst. Growth Des.*, 2010, **10**, 3794–3801.

11 E. Widenkvist, R. A. Quinlan, B. C. Holloway, H. Grennberg and U. Jansson, *Cryst. Growth Des.*, 2008, **8**, 3750–3753.

12 W. Li, C. Liu, Y. Yang, J. Li, Q. Chen and F. Liu, *Mater. Lett.*, 2012, **84**, 41–43.

13 Z. Jiao, J. Wang, L. Ke, X. W. Sun and H. V. Demir, *ACS Appl. Mater. Interfaces*, 2011, **3**, 229–236.

14 N. Wang, D. Wang, M. Li, J. Shi and C. Li, *Nanoscale*, 2014, **6**, 2061–2066.

15 M. F. Daniel, B. Desbat, J. C. Lassegues, B. Gerand and M. Figlarz, *J. Solid State Chem.*, 1987, **67**, 235–247.

16 R. S. Lillard, G. S. Kanner and D. P. Butt, *J. Electrochem. Soc.*, 1998, **145**, 2718–2725.

17 V. S. Vidyarthi, M. Hofmann, A. Savan, K. Sliozberg, D. König, R. Beranek, W. Schuhmann and A. Ludwig, *Int. J. Hydrogen Energy*, 2011, **36**, 4724–4731.

18 B. L. Cushing, V. L. Kolesnichenko and C. J. O'Connor, *Chem. Rev.*, 2004, **104**, 3893–3946.

19 M. S. Elbasiouny, S. A. Hassan and M. M. Hefny, *Corros. Sci.*, 1980, **20**, 909–917.

20 J. Johnson and C. Wu, *J. Electrochem. Soc.*, 1971, **118**, 1909–1912.

21 B. A. Pinaud, P. C. K. Vesborg and T. F. Jaramillo, *J. Phys. Chem. C*, 2012, **116**, 15918–15924.